Article

Not peer-reviewed version

Climatology of Cirrus Clouds over Observatory of Haute-Provence (France) Using Multivariate Analyses on Lidar Profiles

Florian A. Mandija *, Philippe Keckhut, Dunya Alraddawi, Sergey Khaykin, Alain Sarkissian

Posted Date: 9 September 2024

doi: 10.20944/preprints202409.0639.v1

Keywords: cirrus clouds; climatology; threefold classification; ERA5 database; lidar observations

 doi:10.20944/preprints202409.0639.v1

Article

Climatology of Cirrus Clouds over Observatory of Haute-Provence (France) Using Multivariate Analyses on Lidar Profiles

Florian Mandija *, Philippe Keckhut, Dunya Alraddawi, Sergey Khaykin and Alain Sarkissian

Laboratoire Atmosphères, Observations Spatiales (LATMOS), IPSL, UVSQ/Paris-Saclay University, Sorbonne University, CNRS, 78280 Guyancourt, France ; florian.mandija@latmos.ipsl.fr

* Correspondence: florian.mandija@latmos.ipsl.fr; Tel.: (+33 605556870)

Abstract: This study aims the classification of the cirrus clouds over the Observatory of Haute-Provence (OHP) in France. Rayleigh-Mie-Raman lidar measurement altogether with ERA5 dataset, are analyzed in order to provide geometrical morphology and optical cirrus properties over the site. The method of the cirrus cloud climatology presented here, is based on a threefold classification scheme based on the cirrus geometrical and optical properties, and their formation history. Principal component analysis (PCA) and subsequent clustering, result on four morphological cirrus classes, three optical groups, and two origin – related categories. Cirrus clouds occur approximately 37% of the time, with most being single-layered (66.7%). The mean cloud optical depth (COD) is 0.39 ± 0.46, and the mean heights range around 10.8 ± 1.35 km. Thicker tropospheric cirrus are observed under higher temperature and humidity conditions than cirrus observed at the vicinity of the tropopause level. Monthly cirrus occurrences vary irregularly, while seasonal patterns peaking in spring. With respect to the mechanism of the formation, there is found that the majority of cirrus clouds, was of in situ origin. The liquid origin cirrus category consists nearly entirely of thick cirrus. Overall result, suggests that in situ origin thin cirrus, located in the upper-tropospheric and tropopause regions, have the most significant occurrence over the site.

Keywords: cirrus clouds; climatology; classification; lidar measurements; ERA5 database.

1. Introduction

According to International Cloud Atlas of the World Meteorological Organization (WMO), clouds are classified into 10 basic types, grouped further on three major categories; high-level clouds, mid-level clouds and low-level clouds (https://cloudatlas.wmo.int/en/cloud-classification-summary.html). High-level clouds, in turn, are subdivided into three types; cirrus, cirrostratus and cirrocumulus [1].

Cirrus clouds are associated with synoptic scale motions, such as orographic uplift in upper troposphere, frontal uplift, convective systems and large-scale raising [2–9]. In European mid-latitude regions, the prevalent cirrus clouds came through slow updrafts in frontal systems, such as warm conveyor belts, as well as other dynamic phenomena like jet streams, mountain waves, and convection [10]. These comprise both liquid-origin and in situ-origin cirrus [11]. Cirrus clouds are pronominally or entirely composed of non-spherical ice crystals with a variety of shapes [12]. Generally, cirrus clouds have a net warming effect, even though depending on their characteristics.

With respect to optical depth, there are three categories of ice clouds: subvisible (SVS), visible and opaque clouds [13,14]. Many efforts have been made to identify additional classes of cirrus clouds. Thus, a clustering classification technique was used by [15], where up to six classes of clouds were identified based on their optical depth, ranging from thick clouds to very thin clouds, with three classes corresponding to cirrus clouds, which is the focus also of this paper.

Regarding to their formation mechanism, cirrus clouds have been classified as liquid and in situ origin [16–18]. In situ origin cirrus are formed directly from water vapor at $T < -38^{o}C$, $RH_{ice} > 100\%$,

 doi:10.20944/preprints202409.0639.v1

and $RH_w < 100\%$ and liquid-origin cirrus that evolve from freezing of liquid drops in clouds at $T \gtrsim -38^oC$ and $RH_w \sim 100\%$. In situ-origin cirrus are thinner, located at the altitudes where they are formed, whereas liquid-origin cirrus are thicker and uplifted from lower altitudes [9,10,18,19]. Cirrus clouds that originate from liquid, are typically associated with frontal systems (or convection). In contrast, cirrus clouds that form in situ are connected to jet streams, mountain waves, and high-pressure systems [10,20]. In situ cirrus have lower optical depth (up to 1.0), producing slight net warming effect (up to 10 W m^{-2}), while liquid-origin cirrus have higher optical depth (1.0 to 3.0), and a strong net cooling effect (−15 to −250 W·m^{-2}) [17].

Lidar high-resolution measurements of the vertical distribution of clouds, provide unique information (that is not obtained with passive instruments) for developing a climatology of highly detailed cirrus cloud variability [21–30]. Lidar vertical-resolved cloud profiles are used in combination with the meteorological parameters provided by nearby radiosondes or dataset of ERA5, to provide more insights about the cloud properties and thermodynamical conditions.

Numerous studies on cirrus clouds in mid-latitude regions have been conducted [10,13,31–51]. Main findings regarding to cirrus occurrence properties reported by several authors are summarized in Table 1. The majority of studies indicate that cirrus clouds at mid-latitudes are formed at altitudes 9 to 10 km, with very large variability of the geometrical and optical depth. Their mid-cloud temperatures (T) range usually in the interval -50 to -60°C. Usually, a slightly smaller fraction of the subvisible and higher fraction of the visible clouds was observed. In addition, no determined fractions between optical groups were observed in the mid-latitude regions. Nevertheless, no systematic differences were noted between the mid-latitude results and those of other regions when grouped together.

The objective of this study is to synergically classify cirrus clouds according to their morphology, optical properties and formation mechanism. The paper is organized as follows: Sect. 2 presents the instrumentation, characteristics of the data sets used, and the methodology used to evaluate the cirrus properties. Sec. 3 gives the results of the multivariate analysis of the cirrus properties, performing a threefold cloud classification. Sect. 4 summarized the main results.

Table 1. Summarized of the general cirrus results (cloud mean height – CMH), geometrical depth – CGT, optical depth – COD, mid-cloud temperature – T, and the occurrences) reported in other studies. Occurrences are presented as fractions of the total cirrus occurrences, and categorized into groups: sub-visible, visible, and opaque. Criteria for CMH and T, along with the selected lidar ratio (LR) used in various studies for cirrus identification, are also presented here.

Previous results					Criteria			Ref.
CMH (km)	CGT (km)	COD	T (°C)	Occurr. (%)	CMH (km)	T (°C)	LR (sr)	
Mid-latitude regions								
10.3 ± 0.9	2.7 ± 0.9	0.31 ± 0.24	-51± 5.5	53 (3-57-40)	8	-38	25	[31]
7.8 ÷ 11.2	1.2 ÷ 4.3	0.37 ± 0.18	-58 ÷ -36	30 (10-49-41)	–	–	31	[32]
–	–	0.14 ± 0.13	–	30 (36-50-14)	–	-38	–	[33]
10.3 ± 1.2	1.8 ± 1.1	0.36 ± 0.45	-51 ± 8.0	26 (14-48-38)	7	-37	–	[36]
10.0 ± 1.3	1.4 ± 1.3	–	–	39 (20-23-57)	–	-25	18	[37]
9.0 ÷ 10.0	2.1 ÷ 2.4	1.18 ÷ 1.23	-50 ÷ -45	–	–	-37	25	[38]
9.2 ± 1.9	1.6	0.36	–	–	5	-40	–	[39]
9.7 ± 1.6	1.6 ± 1.5	–	-50 ± 9.5	–	7	-25	25	[51]
10.1 ± 1.7	1.6 ± 1.1	0.07 ÷ 0.50	-52 ÷ -38	37 (38-32-30)	–	-25	–	[41]
8.6 ÷ 11.5	0.9 ÷ 3.2	0.13 ÷ 0.80	-58 ÷ -41	47 (23-50-27)	–	–	18	[43]
Other regions								
9.8 ± 1.7	1.5 ± 0.7	0.45 ± 0.30	-39± 5.0	11 (0-80-20)	6	-27	27	[47]
10.0 ± 0.8	1.6 ± 0.7	0.30 ± 0.30	-40± 6.0	64 (2-61-37)	6	-27	27	[47]
12.8 ± 1.5	1.8 ± 1.0	0.28 ± 0.29	-58± 11	43 (8-52-40)	9	–	30	[52]
13.6 ± 2.1	1.4 ± 1.1	0.25 ± 0.46	–	74 (42-38-20)	–	-37	23	[48]

 doi:10.20944/preprints202409.0639.v1

14.7 ± 1.8	1.7	0.33 ± 0.29	-65± 12	15 (16-34-50)	9	-40	28	[49]
–	–	0.37± 0.25	–	–	8	-20	27	[53]
10.1	3.0 ± 0.9	0.26 ± 0.11	-65± 4.0	(0-68-32)	8	–	32	[50]

2. Materials and Methods

2.1. Lidar Description

The lidar instrumentation is very important in the climatological studies, especially of thin or very thin cirrus clouds. Multiple lidar stations have been employed in systematic climatological investigations of cirrus clouds within the midlatitudes. Some of them are located in European sites, such as Haute Provence and Clermont-Ferrand in France, Jülich in Germany, Zürich and Jungfraujoch in Switzerland, Rome Tor Vergata in Italy, etc. [2,32,33,36,41].

Originally designed for Rayleigh scattering to derive temperature and study stratospheric aerosols, the lidar used at this study was enhanced in 1994 with additional channels for water vapor, nitrogen density, and aerosols, facilitating simultaneous cirrus retrieval. The Rayleigh-Mie-Raman lidar, stationed at the Observatory of Haute Provence (site is located at 43.9° N, 5.7° E, and 679 meters altitude), conducts year-round night-time measurements, except during low cloud cover. It typically operates for about 6 hours per session, with varying duration based on factors like cloud cover and operator availability [42,43,54]. This lidar employs a doubled Nd-YAG laser emitting a light pulse of approximately 10 nanoseconds at 532 nm, with a repetition rate of 50 Hz and an average pulse energy of 300 mJ. Backscattered photons are collected using optical fibers. The Nitrogen Raman channel, an upgrade of the Rayleigh temperature lidar within the Network for the Detection of Atmospheric Composition Change (NDACC), utilizes a 20 cm telescope and a 1mm diameter optical fiber [55]. The field-of-view is 1 mrad. The cirrus detection system consists of a primary lens, an interference filter, and a mechanical electric shutter system minimizes noise from the initial burst. Adjusting photon flux optimizes signal quality and retrieval accuracy. To mitigate specular reflections, the lidar beam is angled away from zenith by a few degrees. Lidar observations have a temporal resolution of 160 s and a vertical resolution of 75 m, which is satisfactory to identify different layers and small-scale cirrus.

2.2. Cloud Retrievals

During the period, between 2021 and 2023, the lidar system collected more than 4000 hours of measurements, having a profile for each 160 s. Here, the vertical profile of the lidar back-scattering ratio (BSR) is used to measure the scattering intensity, and the cloud geometrical depth, both are used to determine the cloud optical depth. This parameter is related to the particle scattering efficiency and particle number density.

The process of retrieving cirrus optical depth using lidar involves making certain assumptions. The cloud optical depth was obtained from BSR profiles by the following expression given by [37]. So, the Cloud Optical Depth (COD) at a certain altitude z_o, is given by integrating the total volume scattering coefficient β(z).

$$\boldsymbol{COD(\lambda, z_o)} = \int_{zo}^{\infty} \beta(\lambda, z)\, dz \tag{1}$$

On the other side, the total volume scattering coefficient β(z) is given as the product of total scattering cross section per molecule σ(z) and the molecular number density N(z).

$$\boldsymbol{\beta_{Rayleigh}}(\lambda, z) = n_{air}(z) \cdot \sigma_{Rayleigh}(z) \tag{2}$$

$$\tau(\lambda, z_o) = \eta \cdot (LR)\sigma_{Rayleigh} \int_{zmin}^{zmax} n_{air}(z)[SR(z) - 1]\, dz \tag{3}$$

 doi:10.20944/preprints202409.0639.v1

$$\tau(\lambda, z_o) = \eta \cdot (LR)\sigma_{Rayleigh} \int_{zmin}^{zmax} n_{air}(z) BSR(z)\, dz \quad (4)$$

Tabular values of each, volume scattering coefficient b(z) and the total scattering cross section at several wavelengths, 0.20 – 0.90 mm, have been provided by [56].

The lidar scattering ratio is obtained from the Mie (aerosol) and Rayleigh (molecular) scattering coefficients, and it is usually defined as the ratio of the cirrus backscattering (excluding background aerosol contribution) to the total backscattering:

$$\boldsymbol{SR} = \frac{\boldsymbol{\beta_{aerosol}(\lambda, z) + \beta_{Rayleigh}(\lambda, z)}}{\boldsymbol{\beta_{Rayleigh}(\lambda, z)}} \quad (5)$$

In free-sky conditions, SR is equal to unity. In our case, the wavelength is 532 nm. In this case $\boldsymbol{\sigma(z) = 5.245\ cm^2}$ and $\boldsymbol{\beta(z) = 1.336\ km^{-1}}$.

Mid-cloud height (CMH) is determined using the lidar scattering ratio.

$$\boldsymbol{CMH} = \frac{\int_{z_{base}}^{z_{top}} \boldsymbol{z' \cdot SR(z') \cdot dz'}}{\int_{z_{base}}^{z_{top}} \boldsymbol{SR(z') \cdot dz'}} \quad (6)$$

To construct the cirrus clouds database, a methodology similar to [57] was employed, adjusting integration times based on discontinuities in the optical depth time series. An iterative approach, motivated by [58] was adopted to identify multiple change points within the value series.

Although there is no widely accepted criterion for identifying cirrus clouds, they are discerned based on two criteria: a temperature threshold and a Scattering Ratio above a defined threshold [59]. The temperature threshold and the cloud altitude range even comparable, are not unique throughout the previous studies (Table 1). Temperature thresholds of starting from -25°C up to -38°C have been used by several studies of cirrus clouds [12,27,60,61]. Temperature threshold of -38°C, where ice can nucleate homogenously without the presence of ice-nucleating particles (INPs) is used here [62]. Regarding the cirrus mean altitude, a diapason ranging from 6 to 9 km threshold was applied by [53,60,63], etc. To estimate the cirrus cloud boundaries, a SR threshold was defined as its average plus three times its standard deviation of the background, in this case 17–19 km altitude range [41,43]. Cirrus clouds distant by less than 500 m from each-other are considered as one cirrus cloud layer [31]. Only clouds with vertical extension above 150 m have been taken into account [33,60].

The value of the lidar ratio dominates the error associated with the optical depth determination [64]. For consistent analysis, a constant lidar ratio of 25 sr was used across different cloud types, which is also the case of this study [51,53]. Nevertheless, other papers recommended different values of lidar ratios [36,65,66] (Table 1). Lidar ratio increases with the cloud thickness, ant it is influenced by multiple scattering effects [47]. In addition, a value of η = 0.75 was chosen, introducing an approximate 20% uncertainty in the retrieved optical depth [51].

2.3. Meteorological Retrievals

In view of the fact that cirrus clouds are a product of weather processes that inject water vapor into the dry upper troposphere, which is a strong function of latitude (redistribution of the solar heating) and longitude (due to the circulations features), their properties depend strongly on the measurement location.

Synoptic conditions are retrieved based on the meteorological data such are air temperature, relative humidity, cloud ice water content, atmospheric pressure, vertical velocity, etc. were obtained from ERA5 reanalysis and elaborated thereafter. ERA5 represents the 5th generation of the European Center for Medium-Range Weather Forecasts – ECMWF.

Gridded data provided by ERA5 have a horizontal resolution of 0.25° x 0.25°. It provides vertical coverage between 1000 hPa up to 1 hPa, with a vertical resolution of 37 pressure levels, and hourly temporal resolution [67]. Because the nearest local meteorological measurements were carried out by radio-soundings in Nimes, which is about 100 km away from OHP, the ERA5 reanalysis dataset was more preferable for these analyses.

 doi:10.20944/preprints202409.0639.v1

2.4. Cloud Classifications

Cirrus classification is undertaken in three phases;
Cirrus Classes based on the cloud morphology,
Cirrus Groups based on the optical properties,
Cirrus Categories based on their formation mechanism.

The first classification, is performed by clustering the PCA outputs. PCA is a statistical technique used to simplify a dataset by reducing its dimensionality, which can make data analysis more tractable. Among various statistical methods, PCA is extensively utilized in atmospheric sciences [43,68,69]. A key advantage of PCA is its ability to reproduce nearly all the variability in a dataset with high accuracy by using only a few principal components (PCs). Here, eight original variables such as the base-, mid-, and top-cloud altitudes, mid-cloud temperature, cloud geometrical and optical depths, relative humidity and cloud ice water content, have been transformed into only two meaningful PCs, relating to cloud altitude and depth. The number of PCAs is determined by the Kaiser criterion, which retains only the most important PCs, whose eigenvalues are greater than 1.

Clustering methods such as K-Means and Partitioning Around Medoids (PAM) methods are commonly used for cloud partitions into different groups [43,70,71]. Here, both methods have been applied in order to partition the dataset into four distinct and non-overlapping clusters, characterized by different cloud properties, here called cirrus classes. Determination of the optimal number of clusters is done automatically by the use in combination of the Silhouette, gap statistic and elbow methods [72].

The second cirrus classification, provides three cirrus groups; subvisible (0.03 > COD), thin (0.03 < COD < 0.3) and thick or opaque (COD > 0.3) [73].

Meanwhile, regarding to their mechanism of formation, cirrus clouds have been categorized into slow and fast in situ origin, and liquid – origin as well. This task was undertaken with relevance to the two criteria; optical depth (COD) and ice water content (CIWC) [11,26]. COD thresholds between the three categories are 0.05 and 1.0, using an overall limit of 3.0 in order to exclude aerosol plumes, which are frequent in these latitudes [74,75]. Meanwhile, the threshold of CIWC between in situ and liquid – origin cirrus is 10^{-6} kg·m^{-3}.

3. Results

3.1. Occurrence and Statistical Characteristics of Cirrus Clouds

During the period January 2021 – August 2023, 356 days have been analyzed, on which about 43.3% (154 days) were characterized by cirrus clouds. Similar result was obtained by [41], who evidenced cirrus in 37% of the total observation time, and by [37] on OHP, who reported 54% of cirrus occurrence and 25% of them being subvisible. These differences arise cause of the different definitions of cirrus occurrence.

The majority of these cirrus cases (66.7%) are characterized by a single – layer structure, and only (33.3%) of them have multi – layer structure. A higher single-layer fraction 80% - 20% is reported by [40], and even higher, 89% – 11% by [13]. In the case of double-layer structure, the mean cloud geometrical depth is reduced by 12%. This result is in accordance with a previous study [40], who suggested CGT reduction by 10% in the case of double layer structure.

Mean values of the cloud properties as mean height, geometrical depth and mid-cloud temperature are 10.8, 1.6 km and -54.9°C. Comparable results of CMH and CGT, but lower mid-cloud temperature, have been reported by [13,31,36–38,41]. Mean cloud optical depth found in this study is 0.39 ± 0.46. This result is comparable with the other results in midlatitude regions (0.31 ÷ 0.37) [31,32,36,38]. CGT and COD are linearly fitted by the determination coefficient of R^2=0.56 (Fig. 1), as in other studies [12,14,31,76].

Preprints.org (www.preprints.org) | NOT PEER-REVIEWED | Posted: 9 September 2024 doi:10.20944/preprints202409.0639.v1

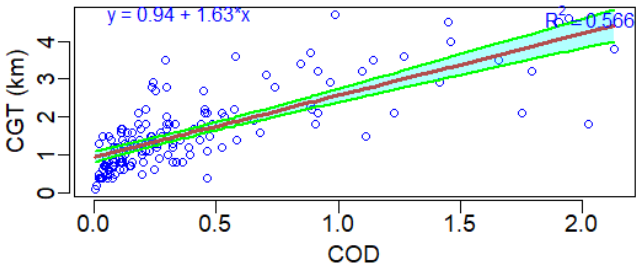

Figure 1. Scatterplot between cloud geometric and optical depth, using the confidence interval of level = 0.95. Also, a regression line, which better fits the data is presented. .

CGT is significantly correlated with COD, by a coefficient of 0.75. Meanwhile, very low correlation was obtained in the case of the dependances of CGT and COD on T and CIWC. Low correlation between COD on CIWC was also obtained. The maximums of these correlations were obtained in the interval -65°C ÷ -45°C, at slightly higher temperatures compared to the tropical regions [77], giving rise to the conclusion that midlatitude cirrus are usually thicker and warmer than tropical cirrus.

3.2. Cirrus Clustering

The very first step in the cirrus characterization and classification is the preliminary study of the probability density functions (PDFs) of the cloud characteristics, such are; cloud base height (CBH), cloud mean height (CMH), cloud top height (CTH), cloud geometrical depth (CGT), cloud optical depth (COD), and mid-cloud temperature (T). PDFs for the above-mentioned cloud parameters are presented in Fig. 2.

The probability distribution functions revealed non-Gaussian multimode distributions, however, characterized by clear principal modes. Table 2 shows all the modes associated by the respective densities.

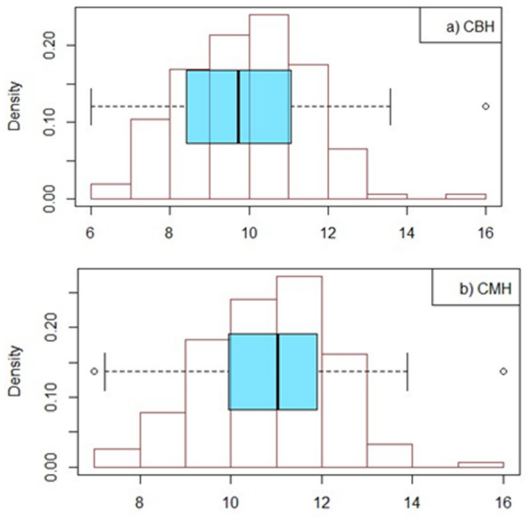

Preprints.org (www.preprints.org) | NOT PEER-REVIEWED | Posted: 9 September 2024 doi:10.20944/preprints202409.0639.v1

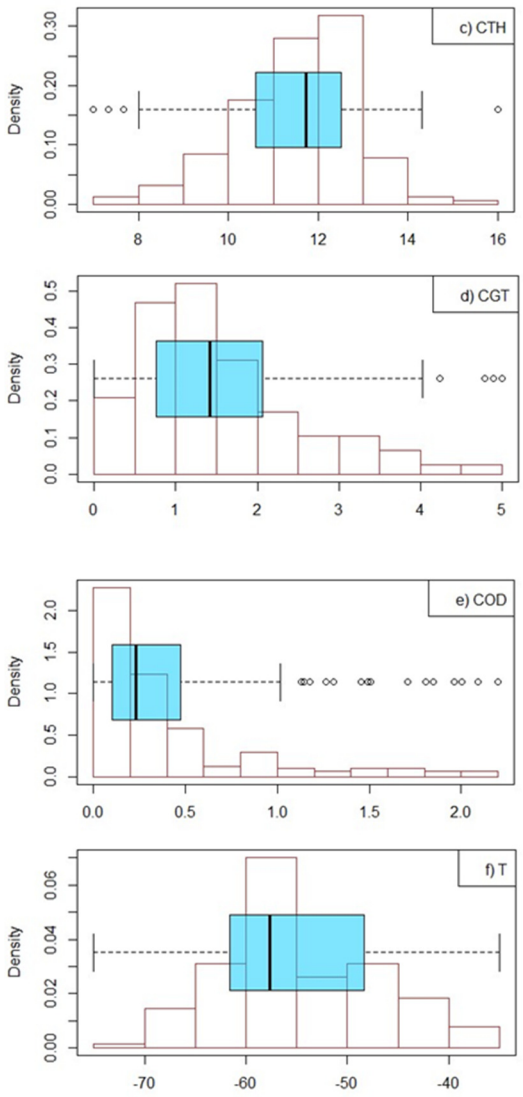

Figure 2. Histograms of PDFs for; cloud base-, mid- and top- heights, cloud geometrical and optical, and mid-cloud temperature. Unimodal and bimodal distributions have been obtained.

Table 2. Principal modes of the distributions of the values of cloud heights, cloud depths, and mid-cloud temperature. In addition, the associated densities of these modes are presented. .

	CBH (km)	CMH (km)	CTH (km)	CGT (km)	COD	T (°C)
1st mode	10.5	11.3	12.2	1.26	0.12	-58.3
1st density	0.24	0.30	0.33	0.49	1.98	0.06
2nd mode	15.2	15.4	15.6	2.94	0.91	-49.2
2nd density	0.005	0.006	0.007	0.10	0. 25	0.03

Interestingly, the distribution of cloud heights shows only unimodal pattern; CBH – 10.5 km, CMH – 11.3 km and CTH – 12.2 km. On the other side, the distributions of the cloud depths, show bimodal pattern; CGT – 1.3 and 2.9 km, and COD – 0.12 and 0.91. Temperature in turn, shows one principal mode (-58.3) and a secondary one (-48.9°C). Furthermore, additional modes of much lower density, have been identified.

In order to make further classification of the cirrus based on their properties, clustering of cloud heights and temperature `have been involved [7,41]. Four clusters were suggested by Silhouette, Elbow and Gap Statistics methods [78]. Mean values of the cirrus properties at these clusters, are shown in Table 3.

 doi:10.20944/preprints202409.0639.v1

Table 3. Cirrus geometrical and optical properties; base-, mid-, and top-cloud height, temperature, geometrical and optical depth, as well as the frequency of occurrences for each cirrus class. Cirrus types based on their thickness and their locations in atmosphere are given.

Class	CBH (km)	CMH (km)	CTH (km)	CGT (km)	COD	T (°C)	Type	Position	Occurr. (%)
K-means method (original data)									
1	11.2	11.7	12.3	1.18	0.23	-64.0	Thin	Tropopause	22.1
2	10.4	11.3	12.2	1.80	0.49	-57.2	Thick	Tropopause	43.5
3	9.3	10.0	10.8	1.58	0.37	-48.4	Moderate	Upper troposphere	23.4
4	7.8	8.6	9.3	1.52	0.37	-41.3	Moderate	Mid-troposphere	11.0
PAM method (original data)									
1	10.7	11.4	12.1	1.40	0.19	-61.3	Moderate	Tropopause	36.6
2	10.2	11.1	11.9	1.70	0.12	-55.6	Thick	Tropopause	30.7
3	9.0	9.8	10.5	1.50	0.24	-47.9	Moderate	Upper troposphere	22.9
4	8.5	8.8	9.0	0.50	0.07	-41.3	Thin	Mid-troposphere	9.8

Cirrus of class 1, found at the highest altitudes, are known as tropopause cirrus clouds. Their mid-cloud height is about 11.5 km. These cirrus clouds are geometrically the thinnest, 1.3 km. Tropopause thin cirrus clouds (similar to class 1) have been found to be associated with large-scale transport processes of moist tropical and sub-tropical air masses named as synoptic cirrus, having relatively short duration, typically less than a day [48].

The thick cirrus of class 2 is situated somewhat at lower heights compared to the first one. This class is geometrically the thickest 1.8 km. Thick low tropopause or/and upper tropospheric cirrus (similar to classes 2 and 3) probably come from standard meteorological phenomena, of large scales fast ascension of warm air masses. The so-called upper-tropospheric cirrus (class 3) is situated at lower altitudes, CMH 10 km, and moderate geometrical depth 1.6 km. Both methods, provide similar occurrence of this class, around 23%.

Cirrus class 4, is the lowest one, in terms of their geometrical heights; CMH 8.7 km. This cirrus class is the less frequent, identified in only about 11% of the cases. Additionally, within the mid-tropospheric cirrus category (similar to class 4), the contribution of contrails can also be anticipated, leading to the formation of what is known as contrail-cirrus. These clouds could be triggered by old and persistent contrails, through the heterogenous nucleation incited by aircraft exhaust. Even the majority of aircraft routes overpass upper tropospheric regions, there aren't ideal conditions for cirrus development. However, mid-tropospheric region over Europe is saturated with respect to ice, which favours the persistence of contrails and the formation of the contrail-cirrus upon the fulfillment of the Schmidt–Appleman criterion [9,46,79–82].

3.3. Principal Component Analysis - PCA

Significative discrepancies between the COD provided by the two clustering methods on original data, makes indispensable the use of the PCA, which generates more consistent outcomes. Furthermore, to reduce the dimensions of the dataset, and remove the strongly correlated variables, PCA is utilized. This technique is also applied successfully in other studies of cirrus climatology [40–44].

In this case, the cloud heights CBH, CMH, CTH, but also the cloud mean temperature result strongly interconnected. Under these conditions, the usage of a new variable, which represents the qualities of these cloud properties is advantageous. In order to establish the optimal number of PCs that adequately explains the variance in the data, the Kaiser criterion is used [83,84].

The eigenvalues of Table 4 show that only the first two PCs both counts on 68.5% of the total variance. To visualize the quality of representation, the scree plot can be used in Fig. 3 [85]. A very similar result was provided by [32,41,43].

Preprints.org (www.preprints.org) | NOT PEER-REVIEWED | Posted: 9 September 2024 doi:10.20944/preprints202409.0639.v1

Table 4. Determination of the number of retained principal components. Eigenvalues corresponding to the amount of the variation explained by each PC. Only PCs with eigenvalues higher than 1, can be taken into account, in this case PC1 and PC2.

	Eigenvalue	Variance (%)	Cumulative variance (%)
PC 1	3.6	44.4	44.4
PC 2	1.9	24.1	68.5
PC 3	1.0	13.1	81.6
PC 4	0.9	11.7	93.3
PC 5	0.3	3.5	96.7
PC 6	0.3	3.3	100
PC 7	3.E-31	4.E-30	100
PC 8	8.E-32	1.E-30	100

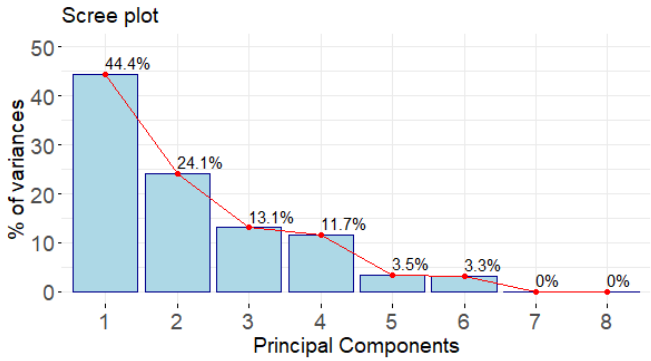

Figure 3. Scree plot, used to visualize the contributions of PCs, on the total variance. The cutoff maybe the first two PCs contributions (68.5%).

The function Cos2 is widely used to determine the quality of representation of a variable on a principal component. For a given variable Xi and a principal component PCj, the function of the Cos2 is calculated by the following equation:

$$\boldsymbol{Cos2(X_i, PC_j) = \left(\frac{coordinate\ of\ X_i on\ PC_j}{\sum_{k=1}^{m} (coordinate\ of\ X_i on\ PC_k)} \right)^2} \quad (7)$$

m is the total number of principal components.

PCs values (Table 5) or Cos2 function (Fig. 4), indicate that PC1 represents better cloud locations (CBH, CMH, CTH and T), PC2 represents better cloud thickness (CGT and COD). On the other side, PC3 represents cloud microphysical properties (CIWC and less RH_w). The remaining PCs (PC4, PC5, PC6, PC7 and PC8) have much less importance, contributing only on 18% of the total variance.

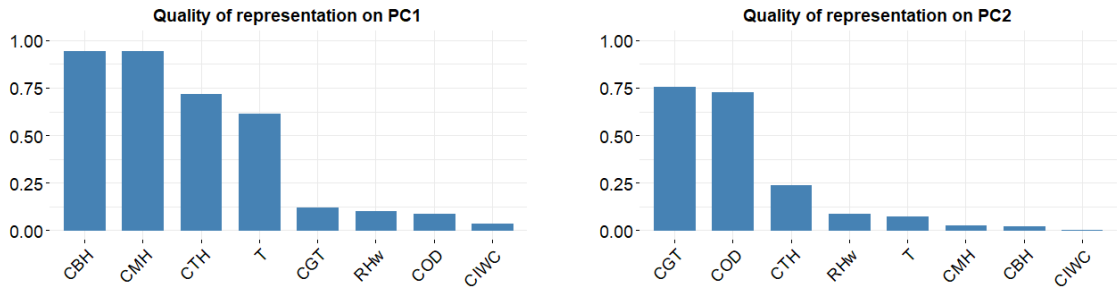

Figure 4. Quality of the representation of all cirrus parameters (CBH, CMH, CTH, CGH, COD, RH_w, T and CIWC) on the two principal components (PC1 and PC2). Cos2 function gives the length of the projection of the cirrus parameters on PCs, so the quality of representation.

Table 5. PCs scores for all the cirrus parameters; CBH, CMH, CTH, CT, COD, T, RH and CIWC. Higher PCs values determine the importance of components at each of the cirrus parameters.

Preprints.org (www.preprints.org) | NOT PEER-REVIEWED | Posted: 9 September 2024 doi:10.20944/preprints202409.0639.v1

	PC1	PC2	PC3	PC4	PC5	PC6	PC7	PC8
Cloud base height (CBH)	0.52	-0.10	0.10	-0.05	-0.30	0.07	0.46	-0.64
Cloud mean height (CMH)	0.51	0.12	0.07	-0.10	-0.16	0.20	-0.80	-0.06
Cloud top height (CTH)	0.45	0.35	0.02	-0.14	0.02	0.33	0.39	0.63
Cloud geometrical depth (CGT)	-0.18	0.63	-0.13	-0.12	0.48	0.34	0.004	-0.44
Cloud optical depth (COD)	-0.16	0.61	-0.12	-0.14	-0.60	-0.45	2E-16	4E-17
Mid-cloud temperature (I)	-0.42	-0.19	-0.07	-0.39	-0.47	0.64	8E-16	7E-16
Relative humidity (RH)	-0.17	0.21	0.54	0.71	-0.22	0.28	3E-16	-1E-16
Cloud ice water content (CIWC)	-0.10	0.02	0.81	-0.53	0.14	-0.18	-6E-17	2E-16
Standard deviation	1.89	1.39	1.02	0.97	0.53	0.51	6.E-16	3.E-16
Proportion of variance	0.44	0.24	0.13	0.12	0.03	0.03	0.E+00	0.00
Cumulative Proportion	0.44	0.68	0.82	0.93	0.97	1.00	1.00	1.00

The biplot of the Fig. 7.a, represents a scatterplot of the PCs scores of the individuals. Meanwhile, the variable loadings of the are plotted as arrows in the Fig. 7.b. Parameters that are grouped together are positively correlated to each other and vice versa. On the other side, the greater the vector is, better that parameter is represented.

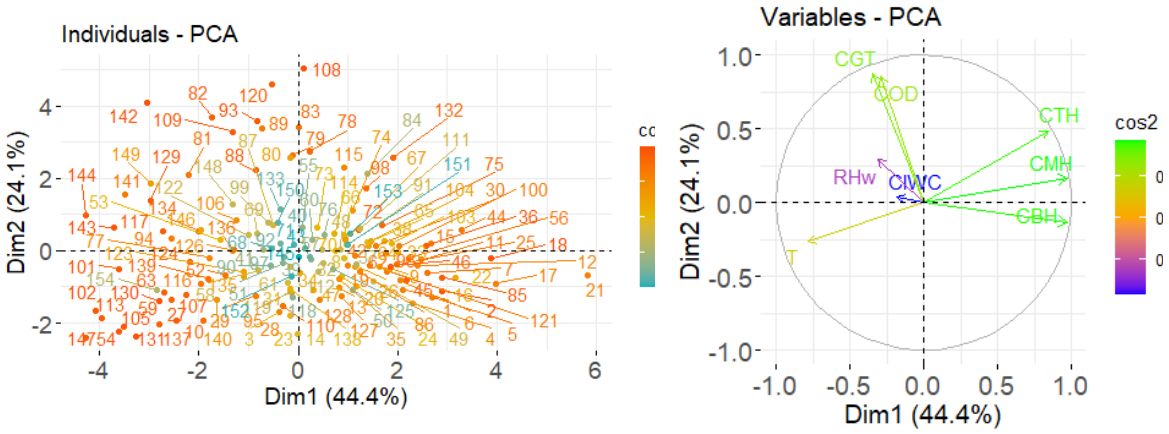

(**a**) (**b**)

Figure 7. Biplots of a) individuals and b) variables. Projection of each of the cloud parameters onto a scatterplot that uses the first two PCs as the axes. Individuals or variables with a similar profile are grouped together. The colors indicate their degree of contribution.

Correlation coefficients calculated by using the original variables and also between PCs according to the list of 154 cirrus cases, are shown also by the correlation matrix, Fig. 8.

Preprints.org (www.preprints.org) | NOT PEER-REVIEWED | Posted: 9 September 2024 doi:10.20944/preprints202409.0639.v1

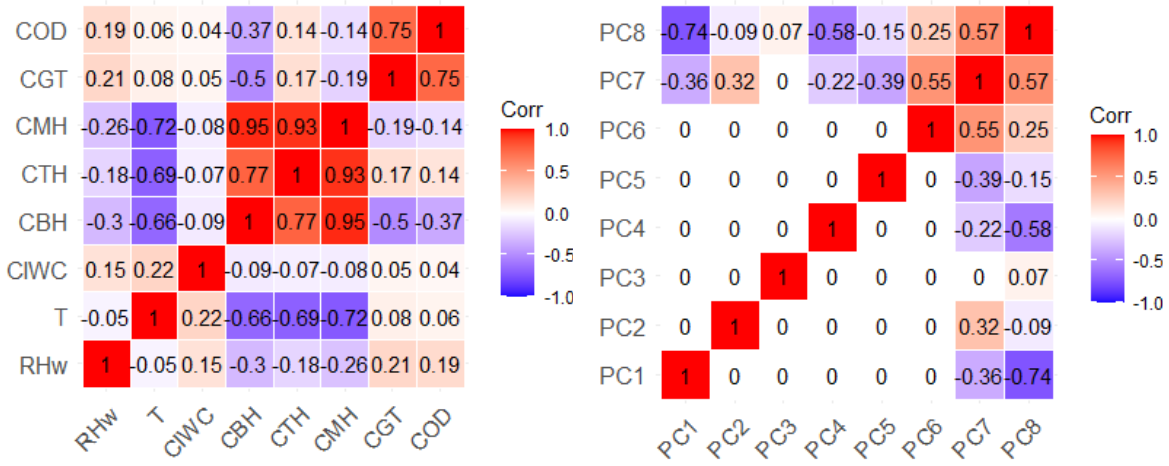

(**a**) (**b**)

Figure 8. a) Pearson correlation matrix among all the variables; temperature, cloud base-, mean- and top heights, geometrical and optical depths, temperature and relative humidity related to water. b) Pearson correlation matrix among the values of the eight principal components.

By comparing the magnitude of the biplot vectors (Fig. 7) and the Pearson correlation coefficients (Fig. 8), cloud altitudes; CBH, CMH and CTH result positively correlated with each other (0.77 ÷ 0.95) and negatively with mid-cloud temperature (-0.66 ÷ 0.72). Furthermore, CGT and COD, result positively correlated with each other (0.75). Cloud ice water content in cirrus results slightly correlated with the relative humidity, as higher RH facilitates the growth of ice crystals, leading to higher CIWC. An interesting but weak correlation, was identified between CBH and COD and CGT, (-0.37 ÷ -0.50). These values indicate that cirrus with elevated base heights tend to be thinner compared to those with low base heights. The other correlations result insignificant, except PC7 and PC8, which are of less importance.

3.4. *Clustering on PCs – Cirrus Classes*

Cluster analysis on the principal components is applied to investigate further cirrus cloud properties and the meteorological parameters. This technique allows us to reduce the amount of excessive data, by using only the less correlated variables (PCs), projecting data onto a lower-dimensional space [86]. Here, the number of variables is reduced from 8 down to 2 (taken in consideration only PC1 and PC2).

According to the majority rule, the optimal number of clusters is between 3 and 5 (Fig. 9). For comparison reasons, PCs have been grouped into 4 clusters, in both clustering methods (Fig. 10). Table 6 summarized the values of the cirrus properties for each class.

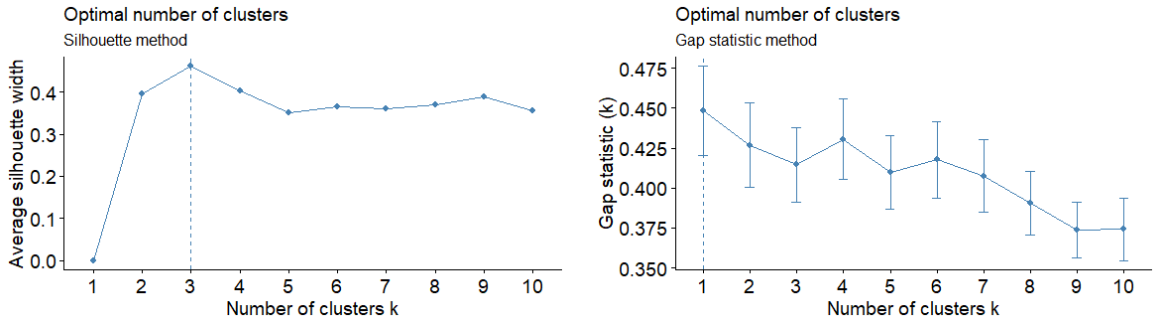

(**a**) (**b**)

Figure 9. Determination of the optimal number of clusters, based on: a) the Silhouette and b) Gap Statistic methods. Silhouette methos suggest 3 optimal clusters, while Gap Statistic method 4.

Preprints.org (www.preprints.org) | NOT PEER-REVIEWED | Posted: 9 September 2024 doi:10.20944/preprints202409.0639.v1

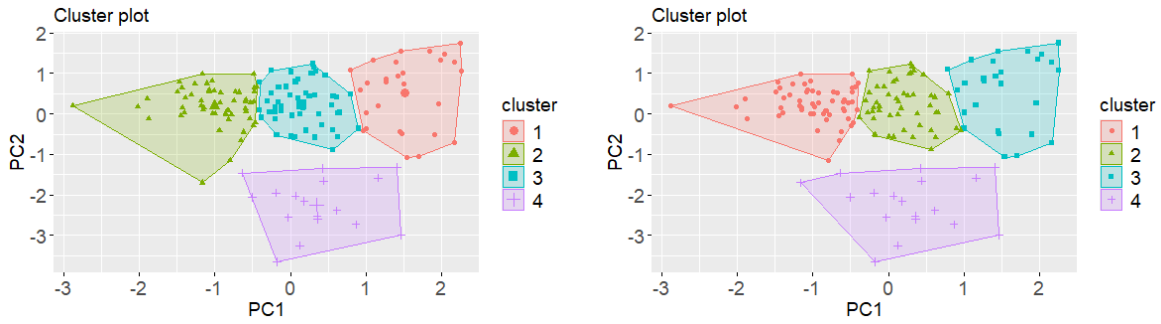

Figure 10. Clustering on PCA results. (a) K-means method and (b) PAM methods, used to discriminate the cirrus data and to group them into four principal classes.

Table 6. Mean properties of the cirrus clouds and their occurrences, classified into four classes. Classification was derived from the clustering on PCA results.

Class	CBH (km)	CMH (km)	CTH (km)	CGT (km)	COD	T (°C)	Type	Position	Occur. (%)
K-means method (original data)									
1	11.7	12.2	12.7	1.06	0.20	-61.3	Thin	Tropopause	31.8
2	9.0	10.7	12.5	3.49	1.39	-55.7	Thick	Upper troposphere	11.7
3	10.0	10.7	11.4	1.43	0.24	-54.7	Moderate	Upper troposphere	37.0
4	8.1	8.8	9.6	1.57	0.40	-44.2	Moderate	Mid-troposphere	19.5
PAM method (original data)									
1	11.52	12.04	12.55	1.03	0.19	-60.9	Thin	Tropopause	37.0
2	9.11	10.84	12.58	3.47	1.41	-56.9	Thick	Upper troposphere	11.7
3	9.75	10.53	11.31	1.56	0.27	-53.4	Moderate	Upper troposphere	33.8
4	8.0	8.7	9.5	1.52	0.39	-43.7	Moderate	Mid-troposphere	17.5

Tropopause cirrus (class 1) are situated in the altitude 12.1 km. This class is the thinnest class in terms of CMH (1.0 km) and COD (0.20). This class is found to be very frequent, about 34%. Upper tropospheric cirrus (class 2) has by far the highest geometrical and optical depths, CGT of 3.5 km and COD of 1.4. However, it is the least common (11.7%). This class is situated in upper troposphere, CMH 10.7 km, same as the class 3. Nevertheless, class 3 is characterized by moderate geometrical depth 1.5 km, low optical depth 0.25, and a high occurrence, 35%. The mid-tropospheric layers (class 4) are situated at the lowest altitudes, CMH is 8.8 km. This class has moderate geometrical depth (1.5 km) and relatively high optical depth (0.40).

Both clustering methods, give approximate results in the case of clustering on PCA results, which was not the case of the original data, where these methods differ too much especially for the COD values. This fact evident another advantage of the method, and strongly recommends of the use of the PCA results instead of the original data. A schematic visualization of the distribution of the four cirrus classes, derived by K-means and PAM methods and using original data and PCA products, are shown in Fig. 10. The classes are better separated in PCA results compared to the original data, which indicates another advantage of the PCA.

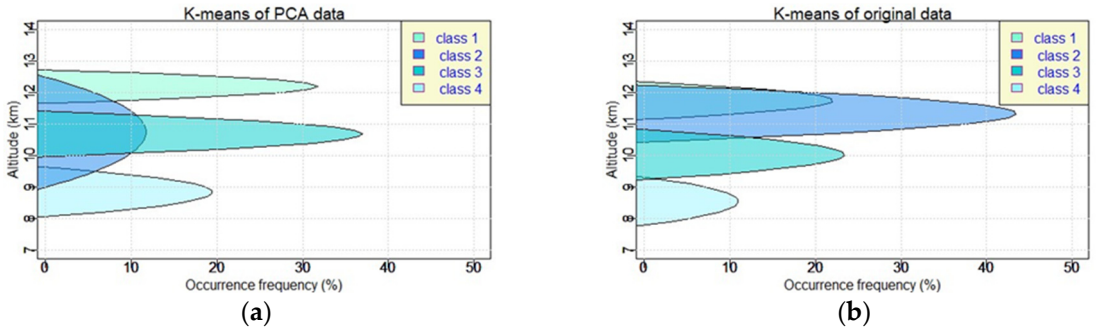

 doi:10.20944/preprints202409.0639.v1

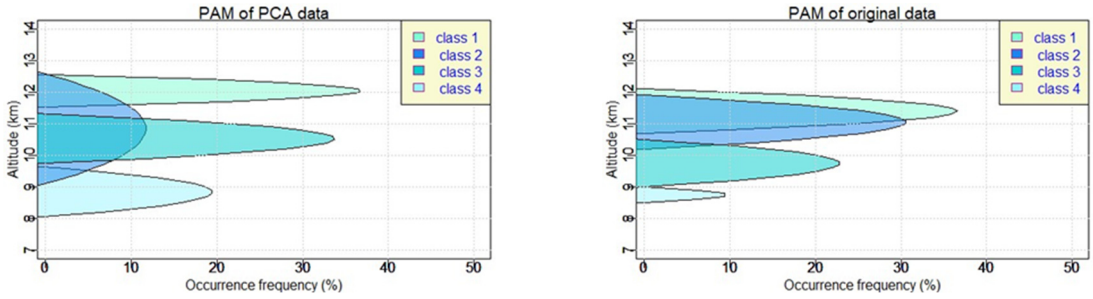

(c) (d)

Figure 11. Patterns of the cirrus classes provided by two clustering methods; K-means and PAM in terms of intensity and occurrence frequency. Visualization based on original data (b., d.) and PCA results (a., c.), using an 2nd degree function as approximation. The function constants have been determined based on the mean values of CMH, CGT and cirrus frequency of occurrences of cirrus.

The result that stands out the most using the PCA results, is the presence of two overlapping cirrus classes (classes 2 and 3). Nevertheless, even these classes have approximate cloud mean heights, their geometrical/optical depths, and also the occurrences, differ too much. Compared to the 3-classes scenario, the use of 4-classes scenario gives additional insights over cirrus layers characteristics on these altitudes, making it advantageous [32]. The four classes information was obtained due to the splitting of the middle class in the previous 3-classes scenario [41,43]. A generalized comparison of the of the cirrus properties, derived by several studies is presented in Table 7.

Table 7. Comparison of cirrus characteristics with previous studies. Here, occurrence, mid- cloud height, geometrical and optical depth, and mid-cloud temperature have been compared.

Characteristic	Ref.	Thin MT	Thick UT	Thin UP	Thin TP
Occurrence (%)	This study	19.5	11.7	31.8	37.0
	[32]	17	21	30	30
	[41]	28	30	42	–
	[43]	36	27	35	–
CMH (km)	This study	8.8 ± 0.9	10.7 ± 0.9	12.2 ± 0.7	10.7 ± 0.6
	[32]	7.8 ± 0.9	8.8 ± 0.9	11.2 ± 0.7	10.2 ± 0.9
	[41]	8.1 ± 1.0	10.4 ± 1.0	11.2 ± 1.1	–
	[43]	8.6 ± 0.9	9.8 ± 0.7	11.5 ± 0.9	–
CGT (km)	This study	1.6 ± 0.7	3.5 ± 0.8	1.1 ± 0.5	1.4 ± 0.5
	[32]	1.2 ± 0.7	4.3 ± 0.8	1.3 ± 0.5	2.8 ± 0.6
	[41]	1.3 ± 0.8	2.9 ± 1	1.0 ± 0.4	–
	[43]	0.9 ± 0.8	3.2 ± 0.9	0.9 ± 0.6	–
COD	This study	0.2 ± 0.8	1.0 ± 0.8	0.1 ± 0.2	0.2 ± 1.0
	[32]	0.04 ± 0.06	0.47 ± 0.36	0.09 ± 0.09	0.16 ± 0.20
	[41]	0.1 ± 0.2	0.5 ± 0.4	0.07 ± 0.06	–
	[43]	0.2 ± 0.2	0.8 ± 0.4	0.1 ± 0.1	–
T (°C)	This study	-44.2 ± 4.0	-55.7 ± 5.1	-61.3 ± 4.2	-54.7 ± 5.0
	[32]	-36 ± 7	-42 ± 7	-58 ± 4	-53 ± 4
	[41]	-38 ± 9	-52 ± 6	-56 ± 7	–
	[43]	-41 ± 6	-50 ± 6	-58 ± 6	–

Statistical interpretation of each of cirrus microphysical properties, is given by the analysis of the box-plots of relative humidity and the cloud ice water content (Fig. 12).

 doi:10.20944/preprints202409.0639.v1

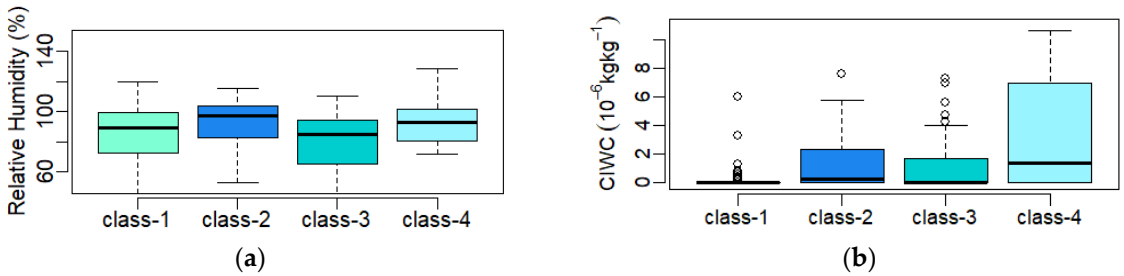

Figure 12. Boxplots of cirrus microphysical properties T, RH, CIWC and COD, for each of the four cirrus classes. .

A strong correlation (0.93) is revealed between the class variation of RH and CIWC values. However, both these microphysical parameters show nonuniform variations along the cirrus classes, with mid-tropospheric cirrus characterized by highest values.

3.5. Optical Properties – Cirrus Groups

Another point of view is the categorization of the cirrus clouds according to their optical properties. In terms of cloud optical depth, three cirrus groups are identified; subvisible, thin and opaque. There are obtained only 5.2% subvisible cirrus (COD < 0.03), 57.1% thin cirrus (0.03 < COD < 0.3) and 37.7% thick cirrus (0.3 < COD). Table 8 shows the comparative results with other studies.

Table 8. Comparison of the percentage fractions among cirrus optical groups from various studies.

SVC	Thin	Thick	Visible	Opaque	Reference
Comparable results					
5	57	38	95	38	This study
3	57	40	97	40	[31]
10	49	41	90	41	[32]
10	65	25	90	25	[90]
14	48	38	86	38	[36]
32	51	17	82	17	[33]
Less similar results					
42	38	20	77	20	[48]
43	46	11	68	11	[33]
35	52	13	62	13	[33]
–	–	–	67	–	[51]
–	–	–	50	–	[13]

The majority of subvisible cirrus are situated at high altitudes. So, 62.5% of them are situated in tropopause (class 1) and 37.5% in the upper troposphere (class 3). Cirrus clouds found at elevated altitudes originate from air masses possessing limited water vapor content, resulting in low geometric and optical depths. Thin clouds are found in 37.5% of the cases in tropopause and in 42.0% in the upper troposphere. Meanwhile, opaque cirrus are found mostly in upper- and mid-troposphere.

Class 1 consists mostly on thin cirrus (67.3%) and less on opaque cirrus (22.4%). Class 2 consists almost completely on opaque cirrus (94.4%). Meanwhile, both thin (opaque) cirrus contributes on classes 3 and 4, by 64.9% (29.8%) and 53.3% (46.7%), respectively.

SVC cirrus are found at the highest altitudes, whilst the opaques the lowest. Regarding cloud depths, CGT and COD display a gradual increase from SVC to opaque cirrus. SVC result to have much lower CIWC compared to visible cirrus.

A compact information in Table 9 shows the parameters of groups. Tropospheric cirrus come out geometrically and optically thicker, and have higher temperature, relative humidity and cloud ice water content, than those situated in tropopause. Especially, upper tropospheric opaque cirrus, have the lowest height, and the highest geometrical and optical depths, temperature and relative

Preprints.org (www.preprints.org) | NOT PEER-REVIEWED | Posted: 9 September 2024 doi:10.20944/preprints202409.0639.v1

humidity. Meanwhile, tropopause CVC clouds, being generally the coldest, and thinnest, exhibit the lowest values of COD and have the lowest RH and CIWC.

Table 9. Mean cloud heights, geometrical and optical depths, cloud ice water content, vertical velocity (ω), mid-cloud temperature and relative humidity (RH), among cirrus optical groups. .

	CBH	CMH	CTH	CGT	COD	CIWC	ω	T	RH
SVC	11.4	11.7	11.9	0.5	0.02	7.4E-07	0.024	-58.8	68.6
Thin	10.3	11.0	11.6	1.2	0.15	2.8E-06	0.015	-54.9	78.3
Opaque	9.3	10.5	11.6	2.3	0.81	2.7E-06	0.004	-54.3	90.3

Even thought, the correlation coefficients of the COD and other properties are statistically low, a significant correlation between COD and CIWC of 0.58 is found for the subvisible cirrus group, which explains the impact of the ice content within the thinnest cirrus on their optical depth. Vertical velocity is very low for both cirrus groups (4-24·10^{-3} ±0.12 Pa·s^{-1}), suggesting a mixing state between ascending and descending motions. Based on the mean vertical velocity, which explains large-scale dynamics of the atmosphere, opaque cirrus clouds result to be characterized by more stable synoptic conditions compared to the thinnest one. Ascending motion will lower the cirrus base height and raise the cloud top, which lift particles to higher altitudes, deepen the supersaturation layer via adiabatic cooling, and maintain the growth of ice crystal particles to larger sizes through the water vapor deposition and aggregation processes until they fall out the supersaturated layer [87].

3.6. Seasonal Variations of the Cirrus Classes and Groups

Because both clustering methods have provided very close results applying on PCA outputs, for simplicity only the k-means will be taken into account in this section. Seasonal occurrences of the cirrus cloud have been analyzed, to have clear picture on their annual variation (Fig. 13).

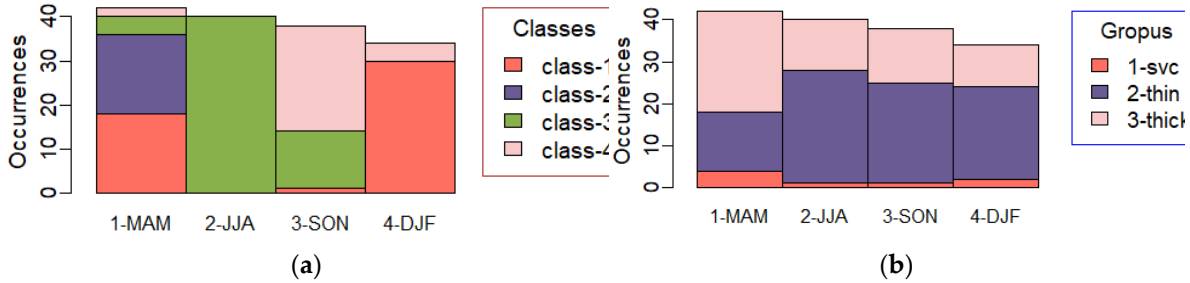

Figure 13. Seasonal variation of the cirrus cloud events over the OHP site. Occurrences of all cirrus cases divided by (a) cirrus classes and (b) cirrus groups, are presented.

The tropopause cirrus clouds are more evident during winter and spring, the upper-tropospheric appears more in summer and less in autumn, while mid-tropospheric cirrus dominate the autumn season. Regarding the seasonal variation in the occurrences of cirrus groups, SVC occurrence remains very low, peaking in spring, similar to the opaque group. Thin cirrus clouds are more frequent during the summer season. Comparable result was obtained also from [36,37,41].

In terms of the monthly variations of all the cirrus classes/groups taken together, two distinct maximums have been observed; in May and during September – October. These two periods correspond to the maximums in spring and autumn seasons, in agreement with satellite climatologies, and suggested by other studies [33,36,41,51]. During winter, low-level clouds often block the laser from reaching potential cirrus clouds, resulting in a lower frequency of lidar measurements [31]. Monthly and seasonal variations of the cirrus occurrences, reveal that the thin tropopause cirrus are strongly affected by the presence of the upper tropospheric cirrus, by reducing deep convection and lidar detection efficiency of high-level clouds [40].

 doi:10.20944/preprints202409.0639.v1

In order to have clear evidence on the seasonal variation of the cirrus properties, there are investigated further the variations of cloud heights, depths and occurrence frequencies according to both the four classes and three cirrus groups (Table 10).

Table 10. Seasonal variations of CBH, CMH, CTH, CGT, COD and T. Also, the seasonal percentage occurrences of each cirrus class and group is presented.

season	CBH (km)	CMH (km)	CTH (km)	CGT (km)	COD	T (°C)	Frequency (%)
MAM	10.2	11.3	12.3	2.06	0.70	-57.8	27.9
JJA	9.9	10.7	11.4	1.50	0.25	-54.5	26.0
SON	8.8	9.5	10.3	1.50	0.34	-47.3	24.7
DJF	11.2	11.8	12.4	1.15	0.23	-60.3	21.4
	Class1	**Class2**	**Class3**	**Class4**	**SVC**	**Thin**	**Opaque**
MAM	12.3	11.7	2.6	1.3	2.6	9.7	15.6
JJA	–	–	26.0	–	0.6	17.5	7.8
SON	–	–	8.4	16.2	0.6	14.9	9.1
DJF	19.5	–	–	1.9	1.3	14.3	5.8

Cirrus heights reach their maxima during the winter – spring seasons, associated with CMH of 11.3 km during MMA and 11.8 km in DJF. The lowest cirrus heights were obtained during autumn; CMH of 9.5 km in autumn. Meanwhile, during the summer season, intermediate cloud heights are more evident. Regarding to the cloud depth, spring season exerts heavily thick cirrus, associated by much higher CGT (2.1 km) and COD (0.70) compared to the other seasons, which in turn have approximate cirrus mean seasonal depths. SVC and opaque, but not thin cirrus, occur mostly in spring. Opaque and SVC cirrus clouds, but not thin ones, are most common in spring.

In the northern mid-latitudes, rapid upward movement of warm air masses, forming thick cirrus clouds, is most frequent in spring. Increased solar heating during this season heightens atmospheric instability, making such phenomena more likely. During spring, stark differences between cold and warm air masses create robust frontal systems and substantial upward movement of warm air.

The atmospheric mechanisms of cirrus formation govern the type of cirrus formed. Thus, sub-visible cirrus clouds are formed because of the cooling near tropopause height, while opaque cirrus clouds are generally formed by deep convective outflow at lower heights except during deep overshooting convections [88]. Summing up, the occurrence of cirrus clouds varies seasonally due to the complex interplay of temperature, humidity, atmospheric circulation, solar radiation, weather patterns, and geographical location. Thus, seasonal variations of temperature, solar radiation, humidity levels, atmospheric general circulation, large-scale weather systems, etc. affect differently the formation of each of the cirrus classes and groups. The orography-driven lifting of air masses leads frequently to lenticularis cirrus. These clouds are thicker than large-scale cirrus clouds but thinner than the cirrus formed as outflow of anvils or in warm conveyor belts.

3.7. Categorization Based on the Cirrus Mechanism of Formation

Other recent studies have included the mechanism of the cirrus formation as a useful tool for their classification. Two main categories have been determined; in situ and liquid origin cirrus [16,19]. Thus, in situ origin cirrus have been sorted out as thin and high cirrus of COD < 1 and CIWC < 10^{-6} kg.m^{-3}, meanwhile, those of liquid origin are thicker and of lower altitude; COD > 1 and CIWC > 10^{-6} kg.m^{-3}. In situ cirrus can be splitted further into two distinct categories; in slow in situ (updraft 10 cm s^{-1}) and fast in situ (updraft 10 cm s^{-1}) [11,16]. Slow in situ have smaller optical depth (COD 0.001–0.05) compared to the fast in situ cirrus (COD 0.05–1.0). According to [19], cirrus clouds formed in situ are more prevalent in temperatures below -55°C, whereas liquid-origin cirrus are more common under higher temperatures.

In addition, the density distribution of the CIWC shows a maximal peak at 9.3E-8 kg·kg^{-1}, which belong mainly to the in situ cirrus, followed by multiple lower peaks at higher CIWC also pertaining

 doi:10.20944/preprints202409.0639.v1

to the liquid – origin cirrus. The mean values of the cirrus properties classified by their mechanism of formation are given in the Table 11.

Table 11. Mean parameters of the cirrus categories; in situ (slow and fast) and liquid – origin cirrus.

	CIWC	CBH	CMH	CTH	CGT	COD	RH	T	Ocurr.
Slow in situ	6.5E-07	11.1	11.4	11.8	0.70	0.05	-57.9	79.4	9.1
Fast in situ	3.4E-07	10.2	11.0	11.8	1.62	0.42	-56.5	80.5	72.1
In situ both	3.8E-07	10.3	11.0	11.8	1.52	0.36	-56.7	80.3	81.2
Liquid origin	8.4E-06	7.8	9.2	10.6	2.78	1.14	-44.3	108.9	5.2
Other cases	1.4E-05	9.5	10.2	10.9	1.48	0.22	-48.4	84.8	13.6

The majority of cirrus clouds, about 72.1% of them result of fast in situ origin, 9.1% of slow in situ, and only 5.2% of liquid origin. Meanwhile, the remaining 13.6% of the cases cannot be classified applying only these conditions, named undefined. Mean values of Table 11 suggest that liquid-origin cirrus have higher CIWC, higher COD, are situated at lower altitudes, at higher temperatures and relative humidity conditions, compared to both in situ cirrus categories.

Liquid – origin cirrus category is composed by only thick cirrus, while in situ cirrus consist of all cirrus groups. Even the slow in situ category doesn't contain opaque cirrus (57% CVC and 43% thin), the fast in situ cirrus are also composed contains by thicker cirrus (57.7% thin and 42.3% opaque).

To have a consideration on this undefined category, the CIWC and COD criteria are taken into consideration. Mean CIWC (1.4E-05 < 1.0E-06) is extremely large, which is a feature of the liquid – origin cirrus. However, the low mean COD (0.22 < 1.0) suggest the in situ origin. The mean altitude (10.2 km) of this category is an intermediate value of the liquid origin (9.2 km) and in situ cirrus (11.0 km), which doesn't allow to have a clear idea of what origin it belongs. The mean temperature (-48.4°C) is lower than the limit of -55°C, which suggest again that the majority of this category belongs to the liquid – origin cirrus [19]. To better categorize this undefined category, a trajectory-based approach is advisable, even though it hasn't been conducted in this study [89].

The frequency distribution of the cirrus cases on their temperature, demonstrates disparities between that of the in situ and cirrus and other cases taken together (Fig. 14). In situ cirrus, both slow and fast, as it is expected, show a distribution peaking at temperatures lower than 50 °C. Meanwhile, the mode of the frequency distribution of other cases (liquid + undetermined) is shifted toward higher temperatures than 50°C, suggesting the predominance of the liquid – origin cirrus. Similar bimodal distribution of temperatures was obtained previously over OHP, situated respectively at -45°C and -60°C [43].

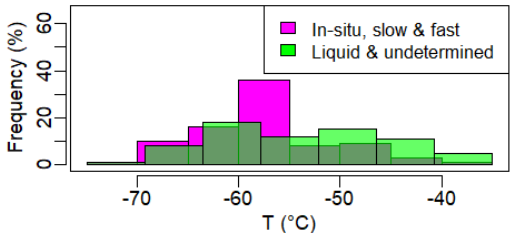

Figure 14. Frequencies of the occurrence of the in situ origin cirrus (comprising the slow and fast uplifting categories), and the liquid origin cirrus (including the other undefined cases). .

At this point, cirrus have been threefold classified with respect of their properties and history. Overall picture of the cirrus triple classification is demonstrated in Table 12.

Preprints.org (www.preprints.org) | NOT PEER-REVIEWED | Posted: 9 September 2024 doi:10.20944/preprints202409.0639.v1

Table 12. General classification scheme of the cirrus clouds based on the three perspectives; cirrus geometrical morphology, optical depth and formation history.

Morphology (4 classes)	Optical properties (3 groups)	Formation mechanisms (3 categories)
Mid-tropospheric	Subvisible	Slow in situ
Thick upper-tropospheric	Thin	Fast in situ
Thin upper-tropospheric	Opaque	Liquid
Tropopause cirrus		

The final results regarding to the main characteristics of the four cirrus classes found beforehand, can be comprised as follows. The mid-tropospheric layer is composed almost by visible cirrus, but of undetermined origin. The thinner upper-tropospheric layer contains mostly thin cirrus (65%) of in situ origin (57%). The thicker upper-tropospheric layer, consists on nearly exclusively opaque cirrus (91%), which has liquid and in situ origin at the same level. The thin upper tropospheric layer, the tropopause cirrus is composed by mainly thin cirrus (62%) of then in situ origin (74%).

To have a better visualization of the co-occurrences among the different cirrus categories, a Chord-Diagram and an Alluvial-Diagram have been created in Figure 15.

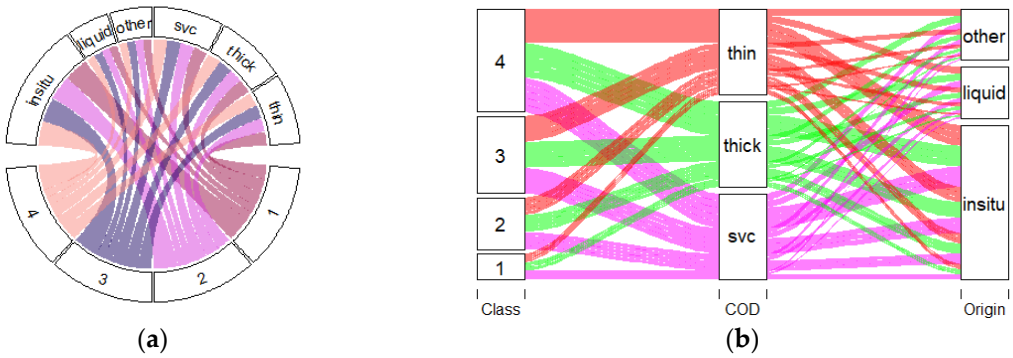

(**a**) (**b**)

Figure 15. Interconnections amon different cirrus categizations. a) Chord-Diagram of the indicating the strength of the relationship between three cirrus classifications. b) Alluvial-Diagram connecting among them, both all cirrus categories. .

Thicker chords of the Chord diagram (Fig. 15.a.) represent stronger connections between categories. It is evident that the strongest relationships are those connecting upper-tropospheric with in situ origin cirrus clouds. After that, very strong correlation demonstrates upper-tropospheric cirrus with thin clouds, and tropopause cirrus with in situ origin clouds. On the other hand, the Alluvia-Diagram of Fig. 15.b. suggest that thin cirrus of the fast in situ origin located in the upper-tropospheric and tropopause regions, have the major coincidence. At European midlatitudes, the most common cirrus clouds are associated with slow updrafts in frontal systems and include both liquid-origin and in situ-origin cirrus [11,16]. However, in this study, fast updrafts in frontal systems reveal to be the most predominant cirrus formation mechanism over OHP.

4. Conclusions

A cross-classifications based on the cirrus cloud geometrical, microphysical and optical properties was performed in this study, utilizing three consecutive years of ground-based lidar measurements carried out at the Observatory of Haute-Provence, France. A multivariate analysis is carried out, combining the cluster analysis with principal component analysis of the cirrus properties. Cloud base-, mid-, and top heights, together with cloud geometrical and optical depths are taken into account. Additional parameters, such as temperature, relative humidity and cloud ice water content, vertical velocity, etc. have been provided by ERA5 reanalysis.

 doi:10.20944/preprints202409.0639.v1

Overall results are comparable with the previous studies in the midlatitude regions, even though new finding have been obtained. One important finding is that clustering on the principal components instead of on the original parameters, gives more accurate and robust results on the classification of the cirrus properties, and makes less determinant the selection of different clustering methods. Cirrus clouds were identified in about 37% of the total observation time. The majority of these cirrus cases (66.7%) are characterized by a single – layer structure, and only (33.3%) of them have multi – layer structure. The mean cloud optical depth found in this study is 0.39. Mean values of the base-, mid- and top cloud height, are 10.0, 10.8 and 11.6 km, respectively. Mid-cloud temperature was -54.9^{o}C. Mean cloud geometrical depth was 1.6 km. High correlations have been estimated between cirrus cloud, base, mid and top height; 0.77 ± 0.95. Also, an inverse-correlated of mid-cloud temperature with all the cloud heights (-0.66 to 0.72). Furthermore, high correlation of 0.75 between geometrical and optical depths was identified as well.

Based on their morphology, cirrus clouds have been classified into four main classes; one mid-tropospheric, two upper-tropospheric and another tropopause cirrus classes. In addition, based on their optical properties, cirrus have been classified into three main groups; subvisible, thin and opaque. The fractions of these cirrus groups are; less subvisible cirrus with 5.2%, more thin cirrus with 57.1%, and 37.7% of thick cirrus. Visible cirrus clouds are the predominant compared to the subvisible cirrus, which are generally situated in the higher altitudes.

The tropospheric cirrus clouds exhibit greater geometric and optical depth, along with higher temperatures, relative humidity, and ice water content compared to those found in the tropopause. Because of the more favorable synoptic conditions, opaque cirrus result more stable compared to the thinner cirrus. Seasonal variations of cirrus occurrences reach a a light maximum during spring. Significant correlations between cirrus classes occurrences reveal that cirrus layers influence each other in multi-layered structures.

In the final step, cirrus clouds have been classified also according to their history of formation. The upper-tropospheric and tropopause thin cirrus belong to the in situ origin, while the opaque upper-tropospheric layer is mainly of uplifted liquid – origin, generally related to the frontal systems. The lowest mid-tropospheric cirrus resulted to be mainly visible but of uncertain mechanism of formation. The most occurring scenario is that of the upper-tropospheric thin cirrus clouds formed in situ.

Acknowledgments: This project has received funding from the French government in the frame of France 2030 under Grant DOS0182433/00 and from the Horizon Europe Research and Innovation Actions program under Grant Agreement N°101056885.

References

1. Sassen, K., Wang, Z. and Liu, D.: Global distribution of cirrus clouds from CloudSat/cloud-aerosol lidar and infrared pathfinder satellite observations (CALIPSO) measurements, J. Geophys. Res.-Atmos., **2008**, 113, D00A12, doi.org/10.1029/2008JD009972.
2. Li, Q., et al. (2005), Convective outflow of South Asian pollution: A global CTM simulation compared with EOS MLS observations, Geophys. Res. Lett., 32, L14826, **2005**, doi:10.1029/2005GL022762.
3. Fu, R., Hu, Y., Wright, J. S., Jiang, J. H., Dickinson, R. E., Chen, M., Filipiak, M., Read, W. G., Waters, J. W., and Wu, D. L.: Short circuit of water vapor and polluted air to the global stratosphere by convective transport over the Tibetan Plateau, P. Natl. Acad. Sci. USA, **2006**, 103, 5664–5669, doi.org/10.1073/pnas.0601584103.
4. Jin, M. L.: MODIS observed seasonal and interannual variations of atmospheric conditions associated with hydrological cycle over Tibetan Plateau, Geophys. Res. Lett., 33, **2006**, L19707, doi.org/10.1029/2006GL026713.
5. Chen, B. and Liu, X.: Seasonal migration of cirrus clouds over the Asian Monsoon regions and the Tibetan Plateau measured from MODIS/Terra, Geophys. Res. Lett., 32, L01804, **2005**, doi.org/10.1029/2004GL020868.
6. Spichtinger, P., Gierens, K., Leiterer, U., and Dier, H.: Ice supersaturation in the tropopause region over Lindenberg, Germany, Meteorol. Z., **2003**, 12, 143–156.
7. Berry E. and Mace, G. G. Cirrus Cloud Properties and the Large-Scale Meteorological Environment: Relationships Derived from A-Train and NCEP–NCAR Reanalysis Data, Journal of Applied Meteorology and Climatology, **2013**, 52, 5; 10.1175/JAMC-D-12-0102.1

8. Muhlbauer, A., T. P. Ackerman, J. M. Comstock, G. S. Diskin, S. M. Evans, R. P. Lawson, and R. T. Marchand, Impact of large-scaledynamics on the microphysical properties of midlatitude cirrus,J. Geophys. Res. Atmos., **2014**, 119, 3976–3996, doi:10.1002/2013JD020035.
9. Wolf, K., Bellouin, N., and Boucher, O.: Long-term upper-troposphere climatology of potential contrail occurrence over the Paris area derived from radiosonde observations, Atmos. Chem. Phys., **2023**, 23, 287–309, https://doi.org/10.5194/acp-23-287-2023.
10. Voigt, C., Schumann, U., Minikin, A., Abdelmonem, A., Afchine, A., Borrmann, S., Boettcher, M., Buchholz, B., Bugliaro, L., Costa, A., Curtius, J., Dollner, M., Dörnbrack, A., Dreiling, V., Ebert, V., Ehrlich, A., Fix, A., Forster, L., Frank, F., Fütterer, D., Giez, A., Graf, K., Grooß, J.-U., Groß, S., Heimerl, K., Heinold, B., Hüneke, T., Järvinen, E., Jurkat, T., Kaufmann, S., Kenntner, M., Klingebiel, M., Klimach, T., Kohl, R., Krämer, M., Krisna, T. C., Luebke, A., Mayer, B., Mertes, S., Molleker, S., Petzold, A., Pfeilsticker, K., Port, M., Rapp, M., Reutter, P., Rolf, C., Rose, D., Sauer, D., Schäfler, A., Schlage, R., Schnaiter, M., Schneider, J., Spelten, N., Spichtinger, P., Stock, P., Walser, A., Weigel, R., Weinzierl, B., Wendisch, M., Werner, F., Wernli, H., Wirth, M., Zahn, A., Ziereis, H., and Zöger, M.: ML-CIRRUS: The airborne experiment on natural cirrus and contrail cirrus with the high-altitude long-range research aircraft HALO, B. Am. Meteorol. Soc., **2017**, 98, 271–288, doi.org/10.1175/BAMS-D-15-00213.1.
11. Krämer, M., Rolf, C., Spelten, N., Afchine, A., Fahey, D., Jensen, E., Khaykin, S., Kuhn, T., Lawson, P., Lykov, A., Pan, L. L., Riese, M., Rollins, A., Stroh, F., Thornberry, T., Wolf, V., Woods, S., Spichtinger, P., Quaas, J., and Sourdeval, O.: A microphysics guide to cirrus – Part 2: Climatologies of clouds and humidity from observations, Atmos. Chem. Phys., **2020**, 20, 12569–12608, doi.org/10.5194/acp-20-12569-2020.
12. Kim, Y, Kim, Sang-Woo, Kim, Man-Hae, Yoon, Soon-Chang. Geometric and optical properties of cirrus clouds inferred from three-year ground-based lidar and CALIOP measurements over Seoul, Korea, Atmospheric Research, **2014**, 139, 27-35.
13. Sassen, K., and J. R. Campbell, A midlatitude cirrus cloud climatology from the facility for atmospheric remote sensing. Part I: Macrophysical and synoptic properties. J. Atmos. Sci., **2001**.a, 58, 481–496.
14. Sassen, K. and Comstock, J. M.: A midlatitude cirrus cloud climatology from the facility for atmospheric remote sensing. Part III: Radiative properties, J. Atmos. Sci., **2001**.b 58, 2113–2127.
15. Desbois, M., G. Seze, and G. Szejwach, Automatic classification of clouds on METEOSAT imagery: Application to high-level clouds. J. Appl. Meteor., **1982**, 21, 401–412.
16. Krämer, M., Rolf, C., Luebke, A., Afchine, A., Spelten, N., Costa, A., Meyer, J., Zöger, M., Smith, J., Herman, R. L., Buchholz, B., Ebert, V., Baumgardner, D., Borrmann, S., Klingebiel, M., and Avallone, L.: A microphysics guide to cirrus clouds – Part 1: Cirrus types, Atmos. Chem. Phys., **2016**, 16, 3463–3483, doi.org/10.5194/acp-16-3463-2016.
17. Luebke, A. E., Afchine, A., Costa, A., Grooß, J.-U., Meyer, J., Rolf, C., Spelten, N., Avallone, L. M., Baumgardner, D., and Krämer, M.: The origin of midlatitude ice clouds and the resulting influence on their microphysical properties, Atmos. Chem. Phys., **2016**, 16, 5793–5809, doi.org/10.5194/acp-16-5793-2016.
18. Wernli, H., Boettcher, M., Joos, H., Miltenberger, A. K., and Spichtinger, P.: A trajectory-based classification of ERA-Interim ice clouds in the region of the North Atlantic storm track, Geophys. Res. Lett., **2016**, 43, 6657–6664, doi.org/10.1002/2016GL068922.
19. Gasparini, B., Meyer, A., Neubauer, D., Münch, S., and Lohmann, U.: Cirrus Cloud Properties as Seen by the CALIPSO Satellite and ECHAM-HAM Global Climate Model, J. Climate, **2018**, 31, 1983–2003, doi.org/10.1175/JCLI-D-16-0608.1.
20. Urbanek, B., Groß, S., Schäfler, A., and Wirth, M.: Determining stages of cirrus evolution: a cloud classification scheme, Atmos. Meas. Tech., **2017,** 10, 1653–1664, https://doi.org/10.5194/amt-10-1653-2017.
21. Klett, J. D.: Stable analytical inversion solution for processing lidar returns, Appl. Opt., 20, 211–220, 1981.
22. Fernald, F. G.: Analysis of atmospheric lidar observations; some comments, Appl. Opt., **1984**, 23, 652–653.
23. Ansmann, A., U. Wandinger, M. Riebesell, C. Weitkamp, and W. Michaelis, Independent measurement of extinction and backscatter profiles in cirrus clouds by using a combined Raman elastic-backscatter lidar, App. Opt., **1992**, 31, 7113-7131.
24. Ansmann, A., J. Bosenberg, G. Brogniez, S. Elouragini, P.H. Flamant, K. Klapheck, H. Linn, L. Menenger, W. Michaelis, M. Riebesell, C. Senif, P.H. Thro, U. Wanclinger, and C. Weitkamp, Lidar network observations of cirrus morphological and scattering properties during the International Cirrus Experiment 1989: J. App. Meteor., **1993**, 3oe, 1608-1622.
25. Gobbi, G. P., Barnaba, F., and Ammannato, L.: The vertical distribution of aerosols, Saharan dust and cirrus clouds in Rome (Italy) in the year 2001, Atmos. Chem. Phys., **2004**, 4, 351–359, doi:10.5194/acp-4-351-2004.
26. Granados-Muñoz, M. J., Navas-Guzmán, F., Bravo-Aranda, J. A., Guerrero-Rascado, J. L., Lyamani, H., Valenzuela, A., Titos, G., Fernández-Gálvez, J., and Alados-Arboledas, L.: Hygroscopic growth of atmospheric aerosol particles based on active remote sensing and radiosounding measurements: selected cases in southeastern Spain, Atmos. Meas. Tech., **2015**, 8, 705–718, doi.org/10.5194/amt-8-705-2015.
27. Comerón, A., Muñoz-Porcar, C., Rodríguez-Gómez, A., Sicard, M., Dios, F., Gil-Díaz, C., dos Santos Oliveira, D. C. F., and Rocadenbosch, F.: An explicit formulation for the retrieval of the overlap function in

an elastic and Raman aerosol lidar, Atmos. Meas. Tech., **2023**, 16, 3015–3025, doi.org/10.5194/amt-16-3015-2023.

28. Granados-Muñoz, M. J., Sicard, M., Papagiannopoulos, N., Barragán, R., Bravo-Aranda, J. A., and Nicolae, D.: Two-dimensional mineral dust radiative effect calculations from CALIPSO observations over Europe, Atmos. Chem. Phys., **2019**, 19, 13157–13173, doi.org/10.5194/acp-19-13157-2019.
29. Mandija, F. Guerrero-Rascado, J. L. Lyamani, H. Granados-Muñoz, M. J. Alados-Arboledas. L. Synergic estimation of columnar integrated aerosol properties and their vertical resolved profiles in respect to the scenarios of dust intrusions over Granada. Atmospheric Environment, 145, 439-454, **2016**.a. doi.org/10.1016/j.atmosenv.2016.09.045.
30. Mandija, F. Markowicz, K. Zawadzka. O. Characterization of aerosol events using synergistically column integrated optical aerosol properties and polarimetric measurements. Journal of Atmospheric and Solar-Terrestrial Physics. 150. 9-20. **2016**.b. doi.org/10.1016/j.jastp.2016.10.012.
31. Giannakaki, E., Balis, D. S., Amiridis, V., and Kazadzis, S.: Optical and geometrical characteristics of cirrus clouds over a Southern European lidar station, Atmos. Chem. Phys., **2007**, 7, 5519–5530, https://doi.org/10.5194/acp-7-5519-2007.
32. Dionisi, Davide, Keckhut, P, Liberti, G. L. Gardillo, F, Congeduti, F. "Midlatitude cirrus classification at Rome Tor Vergata through a multichannel Raman-Mie-Rayleigh lidar." Atmospheric Chemistry and Physics, **2013**, 13, 11853-11868.
33. Kienast-Sjögren, E., Rolf, C., Seifert, P., Krieger, U. K., Luo, B. P., Krämer, M., and Peter, T.: Climatological and radiative properties of midlatitude cirrus clouds derived by automatic evaluation of lidar measurements, Atmos. Chem. Phys., **2016**, 16, 7605–7621, doi.org/10.5194/acp-16-7605-2016.
34. Bartolome Garcia, I., Spang, R., Ungermann, J., Griessbach, S., Krämer, M., Höpfner, M., and Riese, M.: Observation of cirrus clouds with GLORIA during the WISE campaign: detection methods and cirrus characterization, Atmos. Meas. Tech., **2021**, 14, 3153–3168, doi.org/10.5194/amt-14-3153-2021.
35. Voigt, C., Schumann, U., Jessberger, P., Jurkat, T., Petzold, A., Gayet, J.-F., Krämer, M., Thornberry, T., and Fahey, D. W.: Extinction and optical depth of contrails, Geophys. Res. Lett., **2011**, 38, L11806, https://doi.org/10.1029/2011GL047189.
36. Gil-Díaz, C., Sicard, M., Comerón, A., dos Santos Oliveira, D. C. F., Muñoz-Porcar, C., Rodríguez-Gómez, A., Lewis, J. R., Welton, E. J., and Lolli, S.: Geometrical and optical properties of cirrus clouds in Barcelona, Spain: analysis with the two-way transmittance method of 4 years of lidar measurements, Atmos. Meas. Tech., **2024**, 17, 1197–1216, doi.org/10.5194/amt-17-1197-2024.
37. Goldfarb, L., Keckhut, P., Chanin, M.-L., and Hauchecorne, A.: Cirrus climatological results from lidar measurements at OHP (44_ N, 6_ E), Geophys. Res. Lett., **2001**, 28, 1687–1690.
38. Campbell, J. R., Vaughan, M. A., Oo, M., Holz, R. E., Lewis, J. R., and Welton, E. J.: Distinguishing cirrus cloud presence in autonomous lidar measurements, Atmos. Meas. Tech., **2015** 8, 435–449, doi.org/10.5194/amt-8-435-2015.
39. Eguchi, N., Yokota, T. & Inoue, G. Characteristics of cirrus clouds from ICESat/GLAS observations. Geophys. Res. Lett. **2007**, doi.org/10.1029/2007GL029529.
40. Dupont, J.-C., M. Haeffelin, Y. Morille, V. Noël, P. Keckhut, D. Winker, J. Comstock, P. Chervet, and A. Roblin, Macrophysical and optical properties of midlatitude cirrus clouds from four ground-based lidars and collocated CALIOP observations, J. Geophys. Res., **2010**, 115, D00H24, doi:10.1029/2009JD011943.
41. Hoareau, C., Keckhut, P., Noel, V., Chepfer, H., and Baray, J.-L.: A decadal cirrus clouds climatology from ground-based and spaceborne lidars above south of France (43.9◦ N–5.7◦ E), Atmos. Chem. Phys. Discuss., **2013**, 13, 6379–6417, doi:10.5194/acpd-13-6379-2013.
42. Keckhut, P., Hauchecorne, A., Bekki, S., Colette, A., David, C., and Jumelet, J.: Indications of thin cirrus clouds in the stratosphere at mid-latitudes, Atmos. Chem. Phys., **2005**, 5, 3407–3414, doi:10.5194/acp-5-3407-2005.
43. Keckhut, P., Borchi, F., Bekki, S., Hauchecorne, A., and SiLaouina, M.: Cirrus classification at mid-latitude from systematic lidar observations, J. Appl. Meteorol. Clim., **2006**, 45, 249–258.
44. Keckhut, P. Perrin, J-M. Thuillier, G. Hoareau, C. Porteneuve, J. and Montouxc, N. Subgrid-scale cirrus observed by lidar at mid-latitude: variability effects of the cloud optical depth. Journal of Applied Remote Sensing, **2013**, 073530-1 Vol. 7.
45. Montoux, N., P. Keckhut, A. Hauchecorne, J. Jumelet, H. Brogniez and C. David, Isentropic modeling of a cirrus cloud event observed in the midlatitude upper troposphere and lower stratosphere, **2010,** J. Geophys. Res., 115, D02202, doi:10.1029/2009JD011981.
46. Lamquin, N., Stubenrauch, C. J., Gierens, K., Burkhardt, U., and Smit, H.: A global climatology of upper-tropospheric ice supersaturation occurrence inferred from the Atmospheric Infrared Sounder calibrated by MOZAIC, Atmos. Chem. Phys., **2012**, 12, 381–405, doi:10.5194/acp-12-381-2012.
47. Voudouri, K. A., Giannakaki, E., Komppula, M., and Balis, D.: Variability in cirrus cloud properties using a PollyXT Raman lidar over high and tropical latitudes, Atmos. Chem. Phys., **2020**, 20, 4427–4444, doi.org/10.5194/acp-20-4427-2020.

48. Gouveia, D. A., Barja, B., Barbosa, H. M. J., Seifert, P., Baars, H., Pauliquevis, T., and Artaxo, P.: Optical and geometrical properties of cirrus clouds in Amazonia derived from 1 year of groundbased lidar measurements, Atmos. Chem. Phys., **2017**, 17, 3619–3636, doi.org/10.5194/acp-17-3619-2017. Meas. Tech., **2017,** 10, 1653–1664, https://doi.org/10.5194/amt-10-1653-2017.
49. He, Q. S., Li, C. C., Ma, J. Z., Wang, H. Q., Shi, G. M., Liang, Z. R., Luan, Q., Geng, F. H., and Zhou, X. W.: The properties and formation of cirrus clouds over the Tibetan Plateau based on summertime lidar measurements, J. Atmos. Sci., **2013**, 70, 901–915, https://doi.org/10.1175/JAS-D-12-0171.1.
50. Lakkis, S. G., Lavorato, M., Canziani, P., and Lacomi, H.: Lidar observations of cirrus clouds in Buenos Aires, J. Atmos. Sol.-Terr. Phy., **2015**, 130–131, 89–95, https://doi.org/10.1016/j.jastp.2015.05.020.
51. Nohra, R., Parol, F., and Dubuisson, P.: Comparison of Cirrus Cloud Characteristics as Estimated by A Micropulse Ground-Based Lidar and A Spaceborne Lidar CALIOP Datasets Over Lille, France (50.60 N, 3.14 E), EPJ Web Conf., **2016**, 119, 16005.
52. Seifert, P., Ansmann, A., Mu, D., Wandinger, U., Althausen, D., and Heymsfield, A. J.: Cirrus optical properties observed with lidar, radiosonde, and satellite over the tropical Indian Ocean during the aerosol-polluted northeast and clean maritime southwest monsoon, J. Geophys. Res., **2007**, 112, 1–14, doi.org/10.1029/2006JD008352.
53. Yorks, J. E., Hlavka, D. L., Hart, W. D., and McGill, M. J.: Statistics of cloud optical properties from airborne lidar measurements, J. Atmos. Ocean. Tech., **2011**, 28, 869–883, doi.org/10.1175/2011JTECHA1507.1.
54. Sherlock, V., Garnier, A., Hauchecorne, A., and Keckhut, P.: Implementation and validation of a Raman lidar measurement of middle and upper tropospheric water vapour, Appl. Opt., **1999**, 38, 5838–5850.
55. Khaykin S., S. Godin-Beekmann, A. Hauchecorne, J. Pelon, F. Ravetta, P. Keckhut, Stratospheric smoke layer with unprecedentedly high backscatter observed by lidars above southern france, Geophysical Research Letters, American Geophysical Union, **2018**, 45 (3), pp.1639-1646. ⟨10.1002/2017GL076763⟩.
56. Bucholtz, A. Rayleigh-scattering calculations for the terrestrial atmosphere, Appl. Opt. **1995**, 34, 2765-2773.
57. Hoareau, C., Keckhut, P., Baray, J.-L., Sarkissian, A., and Durry, G.: Methodology for water monitoring in the upper troposphere with Raman lidar at Observatory of Haute-Provence, J. Atmos. Ocean. Technol., **2009**, 26, 2149–2160.
58. Lanzante J. R.: Resistant, robust and non-parametric techniques for the analysis of climate data: Theory and examples, including applications to historical radiosonde station data, Int. J. Climatol., **1996**, 16, 1197–1226.
59. Nellore, M.K., Kannan, V., & Vellaisamy, A.L. A Statistical Method for Determining Optical and Geometrical Characteristics of Cirrus Clouds. Climate, **2019**.
60. Li, Q. and Groß, S.: Changes in cirrus cloud properties and occurrence over Europe during the COVID-19-caused air traffic reduction, Atmos. Chem. Phys., **2021**, 21, 14573–14590, doi.org/10.5194/acp-21-14573-2021.
61. Córdoba-Jabonero, C., Lopes, F. J. S., Landulfo, E., Cuevas, E., Ochoa, H., and Gil-Ojeda, M.: Diversity on subtropical and polar cirrus clouds properties as derived from both ground-based lidars and CALIPSO/CALIOP measurements. Atmos. Res., **2017**, 183, 151–165, doi.org/10.1016/j.atmosres.2016.08.015.
62. Gryspeerdt, E., Quaas, J., Goren, T., Klocke, D., and Brueck, M.: An automated cirrus classification, Atmos. Chem. Phys., **2018**, 18, 6157–6169, doi.org/10.5194/acp-18-6157-2018.
63. Dekoutsidis, G., Groß, S., Wirth, M., Krämer, M., and Rolf, C.: Characteristics of supersaturation in midlatitude cirrus clouds and their adjacent cloud-free air, Atmos. Chem. Phys., **2023**, 23, 3103–3117 https://doi.org/10.5194/acp-23-3103-2023.
64. Cadet, B., V. Giraud, M. Haeffelin, P. Keckhut, A. Rechou, and S. Baldy, improved re-trievals of the optical properties of cirrus clouds by a combination of lidar methods, Appl. Opt., **2005**, 44 (9), 1726-1734.
65. Platt, C. M. R. and A. C. Dilley. "Determination of the cirrus particle single-scattering phase function from lidar and solar radiometric data." Applied Optics, **1984**, 23 3, 380.
66. Chen WN, Chiang CW, Nee JB. Lidar ratio and depolarization ratio for cirrus clouds. Appl Opt. **2002** Oct 20;41(30):6470-6. doi: 10.1364/ao.41.006470. PMID: 12396200.
67. Hersbach, H., Bell, B., Berrisford, P., Biavati, G., Horányi, A., Muñoz Sabater, J., Nicolas, J., Peubey, C., Radu, R., Rozum, I., Schepers, D., Simmons, A., Soci, C., Dee, D., Thépaut, J-N. ERA5 hourly data on pressure levels from 1940 to present. Copernicus Climate Change Service (C3S) Climate Data Store (CDS), **2023**, DOI: 10.24381/cds.bd0915c6.
68. Wilks, D. S., Statistical Methods in the Atmospheric Sciences. International Geophysics Series, **1995**, Vol. 59, Academic Press, 464 pp.
69. Shcherbakov , V. , Gayet , J.-F. , Jourdan , O. , Minikin , A. , Ström , J. , & Petzold , A. Assessment of cirrus cloud optical and microphysical data reliability by applying statistical procedures. Journal of Atmospheric and Oceanic Technology, **2005**, 22 (4), 409 – 420.
70. Jeggle, K., Neubauer, D., and Lohmann, U.: Identification of cirrus formation regimes using cluster analysis of back trajectories and satellite data, EGU General Assembly 2023, Vienna, Austria, 24–28 Apr 2023, EGU23-5002, https://doi.org/10.5194/egusphere-egu23-5002, 2023.

71. Gordon, N. D., & Norris, J. R. Cluster analysis of midlatitude oceanic cloud regimes: Mean properties and temperature sensitivity. Atmospheric Chemistry and Physics, 10(13), **2010**, 6435–6459. https://doi.org/10.5194/acp-10-6435-2010.
72. Kurihana, T.; Moyer, E.J.; Foster, I.T. AICCA: AI-Driven Cloud Classification Atlas. Remote Sens. **2022**, 14, 5690. https://doi.org/10.3390/rs14225690.
73. Sassen, K. and Cho, B. Y.: Subvisual-thin cirrus lidar dataset for satellite verification and climatological research, J. Appl. Meteorol., **1992**, 31, 1275–1285.
74. Mandija, F. Sicard, M. Comerón A. Alados-Arboledas, L. Guerrero-Rascado, J. L. Barragan, R. Bravo-Aranda, J.A. Granados-Muñoz, M. J. Lyamani, H. Porcar, C. M. Rocadenbosch Burillo, F. Rodríguez, A. Valenzuela, A. Vizcaíno, D. G. Origin and pathways of the mineral dust transport to two Spanish EARLINET sites: effect on the observed columnar and range-resolved dust optical properties. Atmospheric Research. 187, 69-83. **2017**. doi.org/10.1016/j.atmosres.2016.12.002.
75. Mandija, F. Nieto, V., R. Sicard, M. Danylevsky, V. Anel Cabanelas, J-A. Gimeno. L. The climatology of dust events over European continent using data of the Dust Regional Atmospheric Model. Atmospheric Research. **2018**, 209, 144-162, doi. doi.org/10.1016/j.atmosres.2018.03.006.
76. Reichardt, J.: Optical and Geometrical Properties of Northern Mid-latitude Cirrus Clouds Observed with a UV Raman lidar, Phys. Chem. Earth (B), **1999**, 24, 255–260.
77. Sunilkumar, S. V. and Parameswaran, K. Temperature dependence of tropical cirrus properties and radiative effects, J. Geophys. Res., **2005**, 110, D13205, doi:10.1029/2004JD005426.
78. Gordon, N. D., & Norris, J. R. (2010). Cluster analysis of midlatitude oceanic cloud regimes: Mean properties and temperature sensitivity. Atmospheric Chemistry and Physics, 10(13), 6435–6459. https://doi.org/10.5194/acp-10-6435-2010.
79. Li, Y., Mahnke, C., Rohs, S., Bundke, U., Spelten, N., Dekoutsidis, G., Groß, S., Voigt, C., Schumann, U., Petzold, A., and Krämer, M.: Upper-tropospheric slightly ice-subsaturated regions: frequency of occurrence and statistical evidence for the appearance of contrail cirrus, Atmos. Chem. Phys., **2023**, 23, 2251–2271, doi.org/10.5194/acp-23-2251-2023.
80. Schumann, U., Poll, I., Teoh, R., Koelle, R., Spinielli, E., Molloy, J., Koudis, G. S., Baumann, R., Bugliaro, L., Stettler, M., and Voigt, C.: Air traffic and contrail changes over Europe during COVID-19: a model study, Atmos. Chem. Phys., **2021**, 21, 7429–7450, doi.org/10.5194/acp-21-7429-2021.
81. Schmidt, E.: Die Entstehung von Eisnebel aus den Auspuffgasen von Flugmotoren, in: Deutschen Akademie der Luftfahrtforschung, R. Oldenbourg, **1941**, 5, 44, 1–15.
82. Appleman, H.: The formation of exhaust condensation trails by jet aircraft, B. Am. Meteorol. Soc., **1953**, 34, 14–20, doi.org/10.1175/1520-0477-34.1.14.
83. Kaiser, H. F., The varimax criterion for analytic rotation in factor analysis. Psychometrika, **1958**, 23, 187–200, doi:10.1007/BF02289233.
84. Berry, E., & Mace, G. G. Cirrus cloud properties and the large-scale meteorological environment: Relationships derived from A-train and NCEP-NCAR reanalysis data. Journal of Applied Meteorology and Climatology, **2013**. 52(5), 1253–1276. https://doi.org/10.1175/jamc-d-12-0102.1.
85. Horn, J. L. A rationale and test for the number of factors in factor analysis. Psychometrika, **1965**, 30(2), 179-185.
86. Yeung, Ka Yee, and W. L. Ruzzo. An empirical study on principal component analysis for clustering gene expression data. Technical report, Department of Computer Science and Engineering, University of Washington, **2000**.
87. Ge, J., Zheng, C., Xie, H., Xin, Y., Huang, J.,& Fu, Q. Midlatitude cirrus cloudsat the SACOL site: Macrophysical prop-erties and large-scale atmosphericstates. Journal of Geophysical Research: Atmospheres, **2018**, 123, 2256–2271. https://doi.org/10.1002/2017JD027724.
88. Pandit, A. K., Gadhavi, H. S., Venkat Ratnam, M., Raghunath, K., Rao, S. V. B., and Jayaraman, A.: Long-term trend analysis and climatology of tropical cirrus clouds using 16 years of lidar data set over Southern India, Atmos. Chem. Phys., 15, 13833–13848, https://doi.org/10.5194/acp-15-13833-2015, 2015.
89. Sandhya, M., Sridharan, S., Indira Devi, M., Niranjan, K., and Jayaraman, A.: A case study of formation and maintenance of a lower stratospheric cirrus cloud over the tropics, Ann. Geophys., 33, 599–608, **2015**, https://doi.org/10.5194/angeo-33-599-2015.
90. Wang, Z. and Sassen, K.: Cirrus cloud microphysical property retrieval using lidar and radar measurements: II, Midlatitude cirrus microphysical and radiative properties, J. Atmos. Sci., **2002**, 59, 2291–2302.